Research Square

Preprints are preliminary reports that have not undergone peer review.
They should not be considered conclusive, used to inform clinical practice,
or referenced by the media as validated information.

Digital twin simulation modeling and online optimization of the mandrel feed strategy for profiled ring rolling

Haotian Li
Lianggang Guo
glgglg66@nwpu.edu.cn

Northwestern Polytechnical University State Key Laboratory of Solidification Processing
Hao Deng
Hengjun Luo
Heng Li

Research Article

Keywords: Profiled ring rolling, Mandrel feed strategy, Model predictive control, Digital twin finite element modelling and simulation, AI-driven ring rolling technology

Posted Date: November 20th, 2026

DOI: https://doi.org/10.21203/rs.3.rs-11003106/v1

License: This work is licensed under a Creative Commons Attribution 4.0 International License.
Read Full License

Digital twin simulation modeling and online optimization of the mandrel feed strategy for profiled ring rolling

Abstract

The mandrel feed strategy in profiled ring rolling (PRR) determines the deformation path of the ring and strongly affects both geometric accuracy (roundness) and microstructure (grain size and grain uniformity). However, due to the strong nonlinearity and path dependency of PRR, the evolution of roundness, grain size, and grain uniformity cannot be explicitly modeled. In addition, the complex evolution of ring states leads to stage-dependent control objectives during PRR. These factors make existing predefined mandrel feed strategies ineffective for achieving coordinated control of ring geometry and microstructure. To address this challenge, an artificial neural network-based model predictive control (ANN-MPC) framework for PRR is proposed. The framework predicts the ring's geometric and microstructural states over a finite horizon and optimizes the mandrel feed rate according to predefined objectives. Data-driven state equations are constructed using ANNs with embedded physics constraints, ensuring physically consistent state prediction and control decisions. Considering the path dependency of PRR, a cost function with state-dependent weights is designed. This allows staged priority scheduling among control objectives according to the evolving state risks, thereby achieving coordinated control of roundness, grain size and grain uniformity of the rolled ring. Based on this framework, a digital twin finite element model (DTFEM) is developed for PRR. It continuously monitors, analyzes, and predicts the ring states, and optimizes and executes the mandrel feed strategy online, achieving coordinated control of ring geometry and microstructure within a single simulation. This work provides crucial theoretical and technical support for the research and development of AI-driven ring rolling technology and intelligent ring-rolling equipment.

***Keywords*:** Profiled ring rolling; Mandrel feed strategy; Model predictive control; Digital twin finite element modelling and simulation; AI-driven ring rolling technology

1. Introduction

Profiled ring rolling (PRR) is an efficient and environmentally friendly incremental forming process for manufacturing profiled rings with continuous metal flow lines, high material utilization, and good mechanical properties [1,2]. These advantages have made PRR the dominant manufacturing method for profiled rings [3,4]. Fig. 1 shows the PRR process. During rolling, the combined action of main roll rotation and mandrel radial feed reduces the ring blank thickness, gradually forms the cross-section profile, and increases the ring diameter from D_0 to D_f. Guide rolls maintain rolling stability, while conical rolls and cover

baffles attached to the main roll control ring height and restrain excessive axial spread. Rolling ends when the reference diameter (D) reaches the target value.

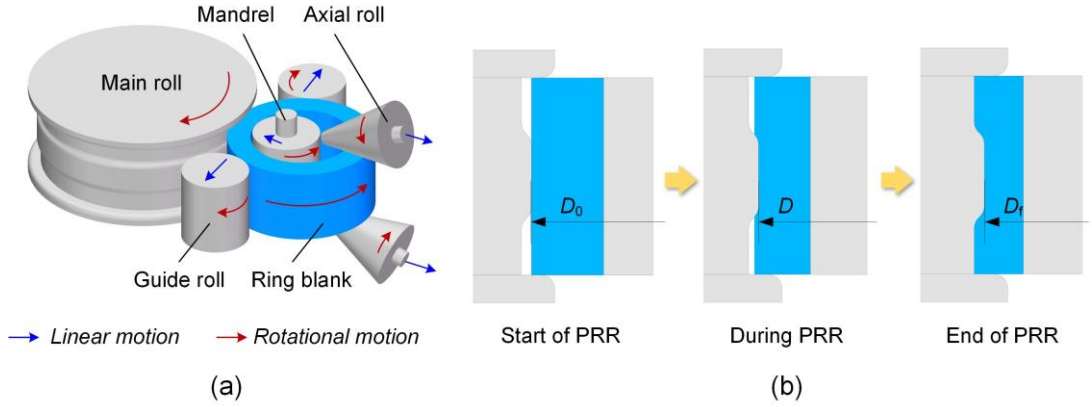

Fig. 1. Schematic diagram of the PRR. (a) Roller motion principle. (b) Evolution of the cross-section profile.

In PRR, the mandrel feed determines the deformation path of the ring and significantly affects its geometric and microstructural evolution [5]. Specifically, it (1) controls the ring diameter expansion rate and process stability [6]; (2) regulates wall-thickness variation between deformed and undeformed regions during each revolution, thereby influencing roundness [7]; (3) modifies the material strain rate, affecting dynamic recrystallization and grain size [8]; and (4) determines the extent of the plastic deformation zone and recrystallization behavior, influencing grain size uniformity [9]. Therefore, the design and optimization of mandrel feed strategies are essential for controlling geometric accuracy (roundness) and the microstructure (grain size and uniformity) in profiled ring manufacturing.

1.1 Review of mandrel feed strategies in PRR

Existing mandrel feed strategies are generally based on two principles. First, the ring outer diameter should expand at a constant rate. Guo et al. [10] demonstrated that a constant diameter expansion rate reduces dynamic impact between the ring and main roll, improving rolling stability and roundness. Second, the mandrel feed rate should satisfy the lower limit required by gripping conditions and the upper limit imposed by forging penetration conditions [11]. These constraints ensure stable ring rotation after gripping and allow the plastic deformation zone to extend throughout the ring cross-section. Based on volume constancy, analytical expressions for the mandrel feed rate were derived [12]. These studies further promoted the development of coordinated multi-roll closed-loop control systems [13] and optimization of roll motion paths [14].

For rings with simple rectangular cross-sections, dimensional evolution during rolling can be directly determined by volume constancy without additional mechanical analysis. However, for profiled rings, complex geometries and deformation behaviors make real-time prediction of dimensional evolution difficult.

Although empirical relationships for mandrel feed rate design can be established for some simple profiles [15], their applicability decreases rapidly with increasing geometric complexity. Therefore, maintaining a constant diameter growth rate through analytical modeling becomes impractical. Instead, empirical feed strategies are commonly adopted, in which the mandrel feed rate decreases progressively with increasing ring diameter to achieve an approximately constant expansion rate [16,17]. To overcome this limitation, Han et al. [18] introduced a proportional-integral-derivative (PID) control algorithm into mandrel feed strategy design. By regulating the diameter growth rate through feedback control, this approach eliminates the need for complex analytical models and makes feed strategy design more efficient. Existing studies on mandrel feed strategies have mainly focused on geometric accuracy, while microstructural quality, another key performance indicator of rolled rings, has received limited attention.

Few studies have incorporated microstructure into mandrel feed strategy design. These studies investigated the effects of mandrel feed rate or ring outer diameter growth rate on temperature, strain, and grain size, and determined optimal predefined feed rates under specific process conditions [8,19]. However, existing strategies mainly rely on offline parameter determination. Obtaining a feed strategy that simultaneously satisfies geometric accuracy and microstructural requirements often requires extensive trial-and-error iterations, limiting the efficient manufacturing of profiled rings. This limitation arises from the complex evolution of geometry and microstructure induced by the strong nonlinearity and path dependency of PRR. Specifically, such state evolution is difficult to model explicitly, and control objectives vary across different forming stages. Therefore, a mandrel feed control framework is needed to monitor geometric and microstructural states in real time and dynamically determine optimal control inputs according to state conditions and stage-specific objectives.

Liang et al. [20,21] developed an intelligent PRR FE model integrating dynamic perception, real-time analysis, autonomous decision-making, and precise execution. During simulation, the model controls roll motions in real time to maintain the ring temperature and forming force within desired ranges. Without predefined rolling trajectories, it can obtain a mandrel feed strategy satisfying temperature and forming force objectives in a single simulation. Although this model cannot simultaneously address multiple constraints, it provides an important reference for the modeling approach of the present work.

1.2 Motivation for optimizing the mandrel feed strategy using ANN-MPC-based digital twin finite element model

To address this challenge, an artificial neural network-based model predictive control (ANN-MPC) framework is proposed. MPC determines control actions by solving online optimization problems over a

finite horizon [22,23]. Its ability to handle multiple constraints and objectives while predicting future system states makes it suitable for incremental forming processes with strong path dependency and evolving control requirements. Wang et al. [24] applied MPC to strip rolling elongation control and reduced elongation fluctuations by optimizing tracking errors and control variations under process constraints. In incremental sheet forming, He et al. [25] and Wang et al. [26] developed switched and online learning-based MPC methods, respectively, achieving improved forming accuracy through predictive error compensation and trajectory optimization. Although MPC has not been applied to PRR, its multi-objective optimization and predictive control capabilities provide a promising solution for coordinated control of geometric accuracy and microstructure.

The strong nonlinearity and path dependency of PRR make analytical modeling of geometric and microstructural evolution difficult, limiting the direct application of MPC. To address this issue, machine learning-based surrogate models have been introduced. Deng et al. [27] developed ANN models to predict geometric evolution in PRR. Lee et al. [28,29] employed extreme gradient boosting and Gaussian process regression for forming force prediction and blank design in ring rolling. Gao et al. [30,31] proposed a digital twin-driven intelligent spinning framework, where a deep neural network-based twin model was combined with PSO for online multi-objective optimization. Xia et al. [32] established a CNN-LSTM model to characterize deformation evolution in multi-pass flow forming and investigated process-defect relationships to suppress defects. Due to their nonlinear approximation capability and compatibility with MPC frameworks [33], ANNs are adopted in this study to predict roundness and grain size evolution in PRR.

In this study, a conventional PRR FE model is coupled with an artificial neural network-based model predictive control (ANN-MPC) controller to establish a material-process-equipment integrated digital twin finite element model (DTFEM), serving as a virtual representation of the physical ring rolling system. The DTFEM integrates the material, process, and control digital twins. The ANN-MPC-based DTFEM optimizes the mandrel feed strategy online within a single simulation, achieving coordinated control of the ring geometry and microstructure.

2. Overview of the ANN-MPC-based digital twin FE model for PRR

2.1 ANN-MPC framework for PRR process

For profiled ring rolling, the evolution of ring geometry and microstructure (ring state) at time instant k+1 is determined by the current ring state and the mandrel feed rate $\boldsymbol{v}_k$ applied at time instant k. The corresponding discrete state equation is given in Eq. (1), where $\boldsymbol{x}$ denotes PRR system state variables, including roundness error, grain size, grain size uniformity, and reference diameter.

$$\boldsymbol{x}_{k+1} = f(\boldsymbol{x}_k, \boldsymbol{v}_k) \tag{1}$$

At each sampling instant k, the current system state is used as the initial condition, and the future evolution of ring geometry and microstructure is predicted over a horizon of length N based on Eq. (1). The optimal control sequence is obtained by solving the optimization problem in Eq. (2), which consists of stage and terminal costs. The stage cost $g(\boldsymbol{x}_{i|k}, \boldsymbol{x}_t, \boldsymbol{v}_{i-1|k})$ penalizes deviations from the target trajectory and regulates transient behavior, where $\boldsymbol{x}_t$, $\boldsymbol{x}_{i|k}$, and $\boldsymbol{v}_{i-1|k}$ denote the target state, predicted state, and control input, respectively. The terminal cost $h(\boldsymbol{x}_{N|k}, \boldsymbol{x}_t)$ ensures convergence to the desired state. The constraint set $\boldsymbol{V}$ incorporates equipment limitations and process requirements, including the allowable mandrel feed rate range and ring quality constraints.

$$\begin{aligned} &\min J(k) = h(\boldsymbol{x}_{N|k}, \boldsymbol{x}_t) + \sum_{i=1}^{N} g(\boldsymbol{x}_{i|k}, \boldsymbol{x}_t, \boldsymbol{v}_{i-1|k}) \\ &s.t. \quad \boldsymbol{v} \in \boldsymbol{V} \end{aligned} \tag{2}$$

Upon solving the optimization problem, an optimal control sequence $\boldsymbol{v}_k^*$ is obtained (Eq. (3)). In practice, only the first element of the optimal control sequence is applied to the system. At the next sampling instant k+1, the system state $\boldsymbol{x}_{k+1}$ is updated based on new measurements, and the optimization problem is re-solved over a shifted prediction horizon. This receding-horizon procedure establishes a closed-loop feedback control framework for online mandrel feed regulation in PRR.

$$\boldsymbol{v}_k^* = [\boldsymbol{v}_{0|k}^*, \boldsymbol{v}_{1|k}^*, \boldsymbol{v}_{2|k}^*, ..., \boldsymbol{v}_{N-1|k}^*]^T \tag{3}$$

2.2 Overall architecture of the ANN-MPC-based DTFEM

Fig. 2 illustrates the architecture of the ANN-MPC-based digital twin finite element model (DTFEM) for PRR. The DTFEM consists of three components: a conventional PRR FE model (Fig. 2(a)), a database (Fig. 2(b)) and an ANN-MPC controller (Fig. 2(c)). The architecture includes two stages: offline construction of the ANN-based system state equations (red arrows in Fig. 2) and online optimization of the mandrel feed strategy (blue arrows in Fig. 2).

In the offline stage, real-time monitoring of ring states during physical PRR remains challenging due to the severe thermo-mechanical conditions and the lack of mature in-situ non-destructive techniques for microstructure characterization. Therefore, the conventional PRR FE model is employed to acquire the evolution data of geometric and microstructural states under different mandrel feed conditions, from which the ANN-based system state equations are constructed. These data are stored in the database and used to train physically constrained ANN models. The development and validation of the FE model, measurement

and evolution of system states, data acquisition and preprocessing are presented in Section 3, and the training and performance evaluation of the ANN models are described in Section 4.

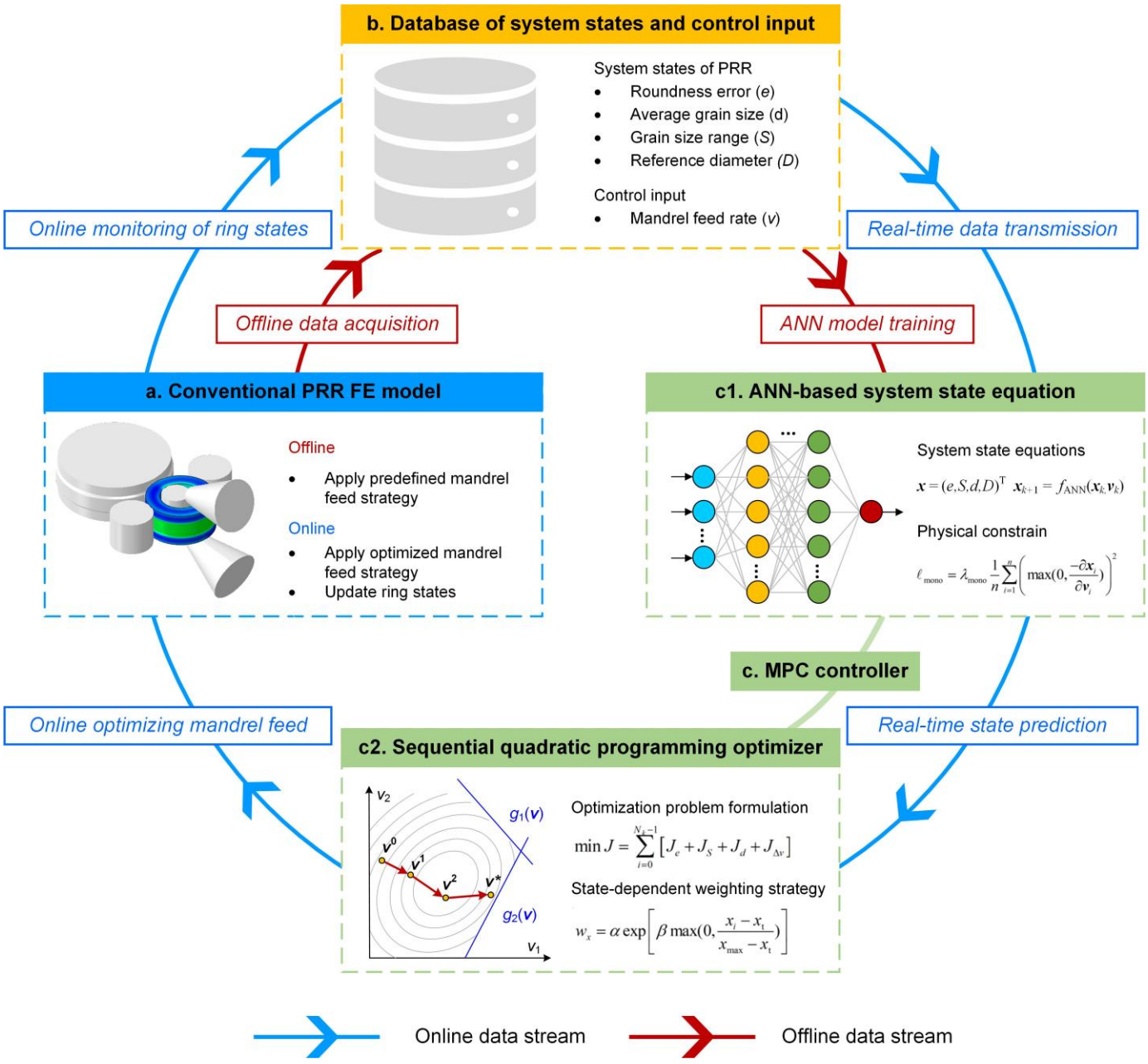

Fig. 2. Architecture and data transfer of the ANN-MPC-based digital twin finite element model for profiled ring rolling.

In the online stage, the mandrel feed strategy is optimized based on the ANN-MPC controller. During PRR simulation, the ring states are continuously monitored and transferred through the database in Fig. 2(b). At each control step, the MPC controller receives the current system states and predicts their future evolution over the prediction horizon using the ANN-based state equations. Subsequently, the nonlinear constrained optimization problem defined in Eq. (2) is solved using the sequential quadratic programming (SQP) algorithm to determine the optimal mandrel feed rate (v) under the specified control objectives. The obtained control input is then applied to the FE model, updating the subsequent ring states evolution and enabling online optimization of the mandrel feed strategy within a single simulation. The solution of the multi-

objective mandrel feed rate optimization problem is presented in Section 5. Finally, Section 6 presents the development of the ANN-MPC-based DTFEM and its application to online optimization of the mandrel feed strategy.

3. Data acquisition and formulation of the PRR system state equation

3.1 FE model of PRR for data acquisition

In this study, a PRR FE model is developed using the ABAQUS platform. Roller motions are adaptively controlled through a VUAMP subroutine, and the constitutive model and recrystallization behavior from Liang et al. [34] are implemented via a VUMAT subroutine. The reliability of the FE model was verified in our previous work, as shown in Fig. 3. A groove-section profiled ring made of IN718 alloy is selected as the study subject, and the simulation parameters are listed in Table 1 [8,17]. Fig. 3(b) and (c) compare the simulated diameter evolution with the experimental results, showing good agreement and confirming the accuracy of geometric prediction. Fig. 3(d) and (e) compare the simulated and experimental grain sizes and corresponding microstructures, demonstrating the capability of the FE model to predict microstructure evolution. Therefore, the validated FE model serves as the controlled object and provides training data for the ANN model.

Table 1. The parameters used in the FE simulation[8, 17].

Parameters	**Values**	**Parameters**	**Values**
Diameter of main roll (mm)	1140	**Environment temperature (°C)**	30
Diameter of mandrel (mm)	320	**Thermal conductivity coefficient (W/(m^2·K))**	5000
Diameter of guide roll (mm)	360	**Convection coefficient (W/(m^2·K))**	20
Cone angle of axial rolls (°)	32	**Emissivity (W/(m^2·K^4))**	0.7
Die temperature (°C)	150	**Friction coefficient**	0.3
Blank temperature (°C)	1000	**Sampling interval (s)**	0.3
Feed rate of mandrel (mm/s)	0.3	**Rotational speed of main roll (rad/s)**	1.1

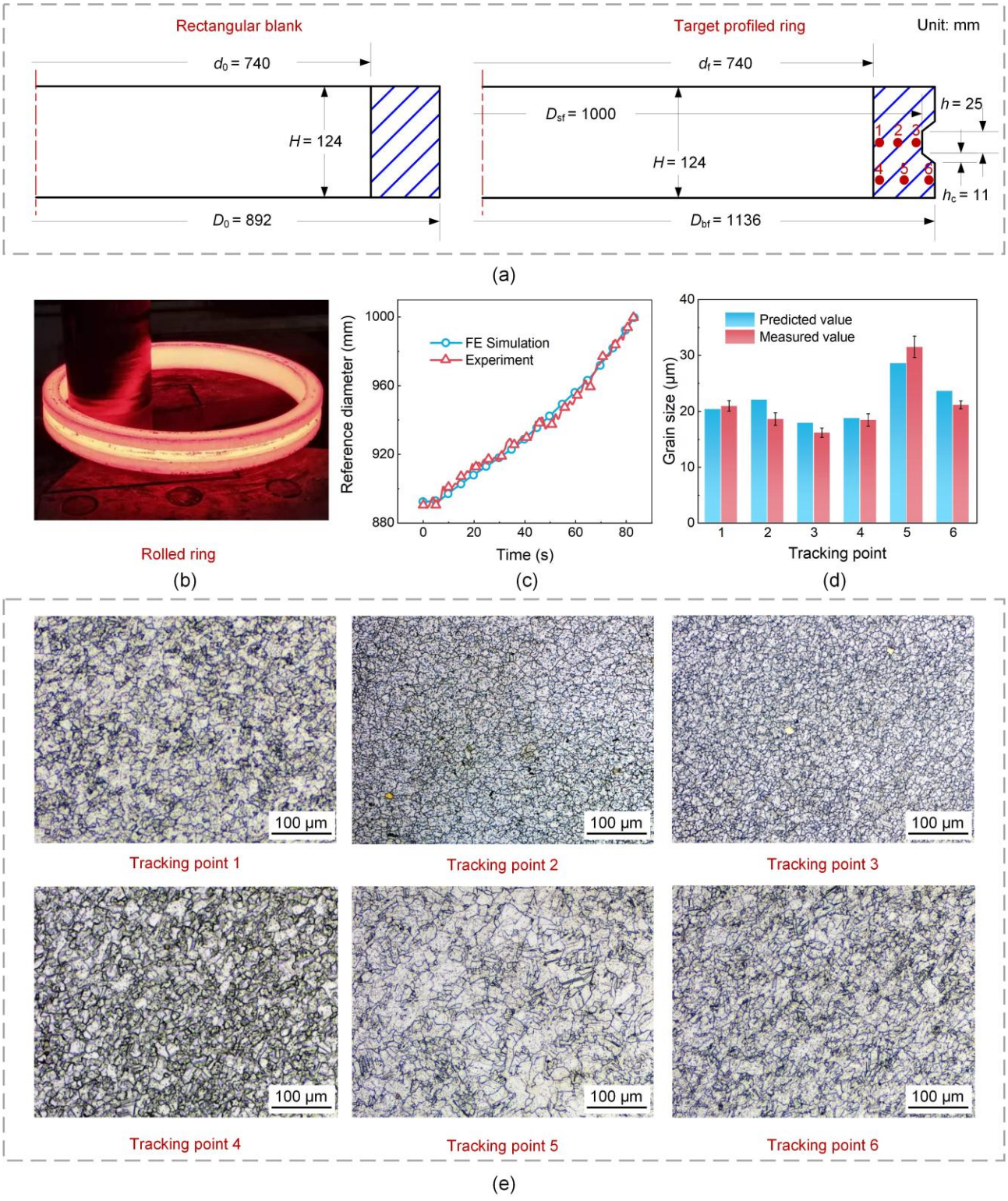

Fig. 3. Verification of the PRR FE model [15, 34]. (a) Blank and target ring. (b) Experimental result of rolled ring. (c) Comparison of outer diameter between simulated and experimental results. (d) Comparison between predicted and measured values of average grain size at each tracking point in (a). (e) Microstructure of each tracking point in (a).

3.2 Measurement and evolution of PRR system states

The system states considered in this study include roundness error, average grain size, grain size range, and reference outer diameter. The roundness error (e), average grain size (d), and grain size range (S) are used to quantify roundness, grain size, and grain uniformity, respectively. The reference diameter (D) is included to track forming progress and geometric evolution but is not a direct control objective. It is

determined using the least-squares method, with the measurement location shown in Fig. 1. The only control input is the mandrel feed rate (v). For convenience, subsequent system states refer to e, S, and d.

Fig. 4(a) shows the initial blank and target ring geometries. To investigate the relationship between v and the system states, four FE simulations are conducted with mandrel feed rates of 1.0, 1.5, 2.0, and 2.5 mm/s. Other parameters are consistent with Table 1. The measurement methods and evolution characteristics of e, S, and d are described in the following subsections.

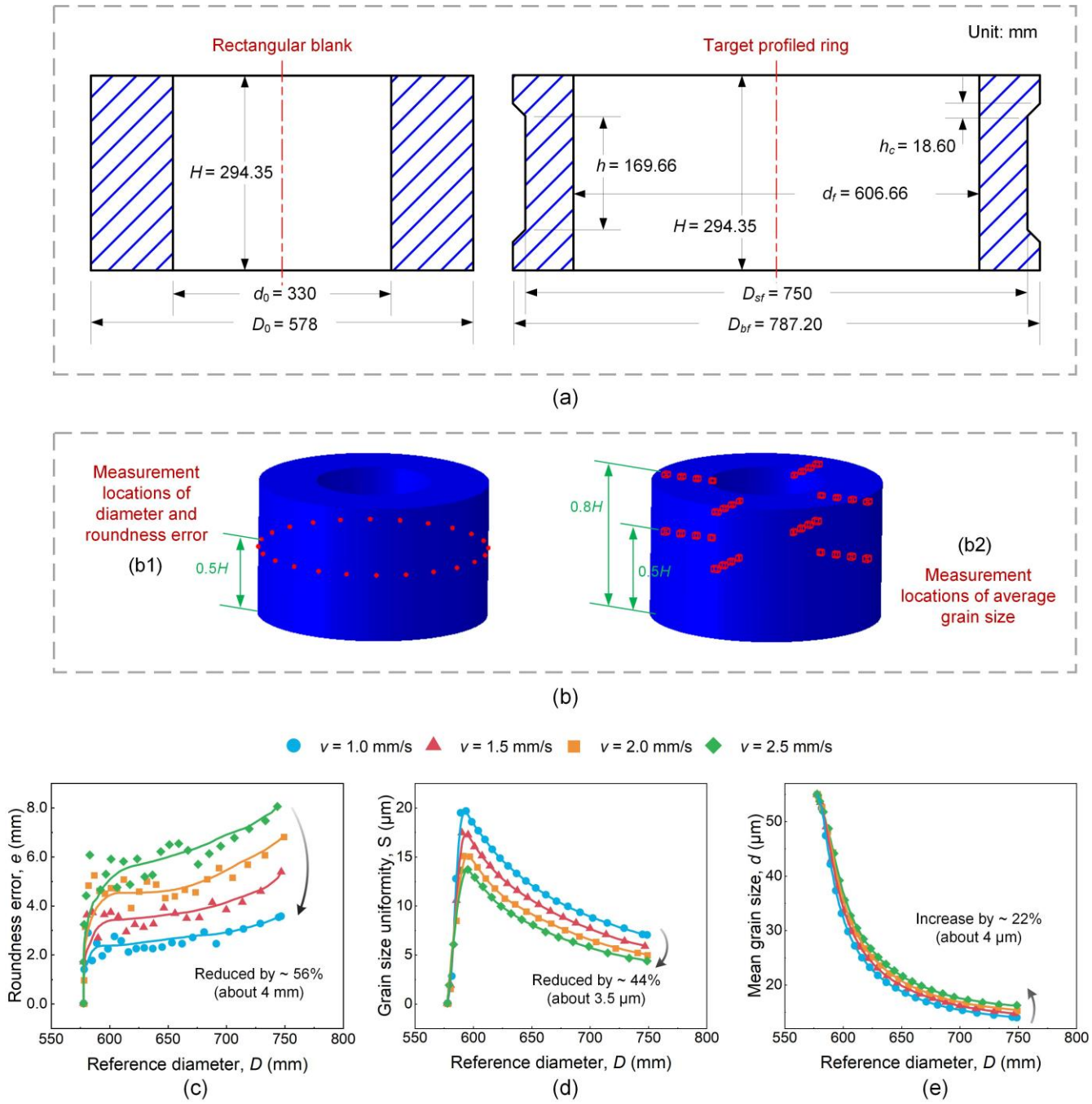

Fig. 4. Evolution of the system states during the PRR process. (a) Initial blank and target ring geometries. (b) Measurement location for roundness error e, grain size range S, and average grain size d. (c) Evolution of roundness error e with respect to reference diameter D. (d) Evolution of grain size range S with respect to reference diameter D. (e) Evolution of average grain size d with respect to reference diameter D.

3.2.1 Roundness error

The roundness error represents the deviation of the ring cross-section contour from an ideal circle. In this work, it is defined as the difference between the maximum and minimum diameters (D_{max} - D_{min}) of the actual contour, as expressed in Eq. (4). The measurement locations of the reference diameter and roundness error are shown in Fig. 4(b1). Fig. 4(c) presents the evolution of e under different v. The roundness error increases continuously during forming and strongly depends on the mandrel feed rate. A higher feed rate leads to a larger roundness error at the same reference diameter, and the increase becomes more pronounced in the later forming stage. These results indicate that reducing the mandrel feed rate, particularly in the final stage, is beneficial for roundness control.

$$e = D_{max} - D_{min} \tag{4}$$

3.2.2 Grain size range and average grain size

As shown in Fig. 4(b2), the grain sizes at four measurement points with the same radial position are averaged. The grain size range S is defined as the difference between the maximum and minimum values among the eight averaged grain sizes across the ring section (Eq. (5)). Fig. 4(d) shows the evolution of S with reference diameter D under different v. A significant increase in S occurs during the initial rolling stage due to non-uniform deformation across the ring section. The surface region reaches the critical strain for dynamic recrystallization earlier than the core region, resulting in faster grain refinement. As deformation penetrates the ring thickness, strain distribution becomes more uniform, reducing grain size differences and causing S to decrease toward a stable level. A higher mandrel feed rate promotes deformation penetration and strain homogenization, thereby reducing S. These results indicate that a relatively high mandrel feed rate in the early stage benefits grain size uniformity.

$$S = d_{max} - d_{min} \tag{5}$$

The measurement locations for the average grain size d are shown in Fig. 4(b2). Fig. 4(e) presents the evolution of d with D under different v. During rolling, d decreases continuously due to dynamic recrystallization and gradually stabilizes as recrystallization approaches saturation. A higher mandrel feed rate results in a larger d because the increased strain rate suppresses dynamic recrystallization. These results indicate that a relatively low v in the early rolling stage promotes grain refinement.

3.3 General form of the system state equation in PRR

PRR is a highly path-dependent process. Therefore, the system state at time k+1 is expressed as a function of the reference diameter, mandrel feed rate, and system state at time k, as defined in Eqs. (6)-(8).

For fixed blank and target ring geometries and main roll speed, the reference diameter D is the only evolving geometric variable during PRR [35]. Thus, other geometric parameters, such as inner diameter and groove depth, are not explicitly included in the state equations. In these equations, f, g, and h denote the unknown nonlinear functions governing the evolution of the system states. Three ANN-based surrogate models are developed and trained in MATLAB to approximate these functions and provide recursive state predictions for the MPC framework.

$$e_{k+1} = e_k + f(v_k, D_k, e_k)(D_{k+1} - D_k) \tag{6}$$

$$S_{k+1} = S_k + g(v_k, D_k, S_k)(D_{k+1} - D_k) \tag{7}$$

$$d_{k+1} = d_k + h(v_k, D_k, d_k)(D_{k+1} - D_k) \tag{8}$$

3.4 Data acquisition and preprocessing

The ANN training data were obtained from a series of FE simulations based on the validated model described in Section 3.1. To capture state evolution under variable v and cover the parameter space, six linearly varying mandrel feed strategies were designed. The first three curves decrease linearly from 2.5 mm/s (the maximum feed rate) to 1.5 mm/s, 1.0 mm/s, and 0.5 mm/s (the minimum feed rate), respectively. The remaining three curves decrease linearly from 2.0 mm/s, 1.5 mm/s, and 1.0 mm/s to 0.5 mm/s, respectively. All other simulation parameters are identical to those described in Section 3.1.

The measurement locations and data acquisition procedures are consistent with those in Section 3.2. To reduce numerical fluctuations caused by small diameter increments, the raw data were averaged over 10 mm diameter intervals. The averaged state variables within each interval were used as ANN training samples. Furthermore, approximately 1500 samples were smoothed using a moving-average filter to reduce noise. The constant-feed simulations in Section 3.2, with feed rates of 1.0, 1.5, and 2.5 mm/s, were also included in the training dataset, enabling the ANN models to capture state evolution under both variable and constant feed conditions.

4. ANN model training and feasibility assessment

4.1 ANN model training

The neural networks are trained using the adaptive moment estimation (Adam) optimizer with the rectified linear unit (ReLU) as the activation function. The maximum number of training epochs is set to 1000, and early stopping is employed when the validation loss fails to decrease for ten consecutive epochs. The loss function is based on the mean squared error (MSE).

To improve the physical consistency and generalization of the ANN surrogate models in MPC,

monotonicity constraints are incorporated into the loss functions based on the state evolution characteristics identified in Section 3.2 and PRR domain knowledge. Specifically, e and d increase with v, whereas S decreases with v. Violations of these relationships are detected by the ReLU function and penalized during training, enabling the MPC controller to generate physically consistent control actions. The loss functions of the three ANN models are given in Eqs. (9)-(11), where n denotes the number of samples and λ_{mono} represents the monotonicity penalty weight. The network architectures and hyperparameters are listed in Table 2.

$$\ell_e = \frac{1}{n}\sum_{i=1}^{n}\left(\frac{\Delta e_i}{\Delta D_i} - \frac{\Delta e}{\Delta D}\right)^2 + \lambda_{mono}\frac{1}{n}\sum_{i=1}^{n}\left(\max\left(0, \frac{-\partial e_i}{\partial v_i}\right)\right)^2 \tag{9}$$

$$\ell_S = \frac{1}{n}\sum_{i=1}^{n}\left(\frac{\Delta S_i}{\Delta D_i} - \frac{\Delta S}{\Delta D}\right)^2 + \lambda_{mono}\frac{1}{n}\sum_{i=1}^{n}\left(\max\left(0, \frac{\partial S_i}{\partial v_i}\right)\right)^2 \tag{10}$$

$$\ell_d = \frac{1}{n}\sum_{i=1}^{n}\left(\frac{\Delta d_i}{\Delta D_i} - \frac{\Delta d}{\Delta D}\right)^2 + \lambda_{mono}\frac{1}{n}\sum_{i=1}^{n}\left(\max\left(0, \frac{-\partial d_i}{\partial v_i}\right)\right)^2 \tag{11}$$

Table 2. Parameters for the ANN models.

Output of ANN	**Number of hidden layers**	**Total number of neurons**	**Data split ratio (training/testing)**	**Weight of the monotonicity constraint, λ_{mono}**
Roundness error, *e*	4	60	0.7/0.3	10
Grain range, *S*	5	84	0.7/0.3	10
Mean grain size, *d*	3	28	0.7/0.3	10

4.2 Performance and interpretability of the ANN model

The training results of the ANN models are presented in Fig. 5. As shown in Fig. 5(a)-(c), the predicted values agree well with the true values. Fig. 5(d)-(f) show that all models achieve $R^2 > 0.9$ with low MAE and RMSE values, indicating high prediction accuracy. The consistent performance between training and test sets further demonstrates good generalization without evident overfitting.

SHAP analysis was performed to interpret the ANN-based incremental state equations in Eqs. (6)-(8), and the results are presented in Fig. 6. Fig. 6(a), (c), and (e) show the feature importance rankings of the three models. For all models, historical system states exhibit the highest importance because the incremental state formulation captures accumulated deformation history, making previous states strongly correlated with the current state.

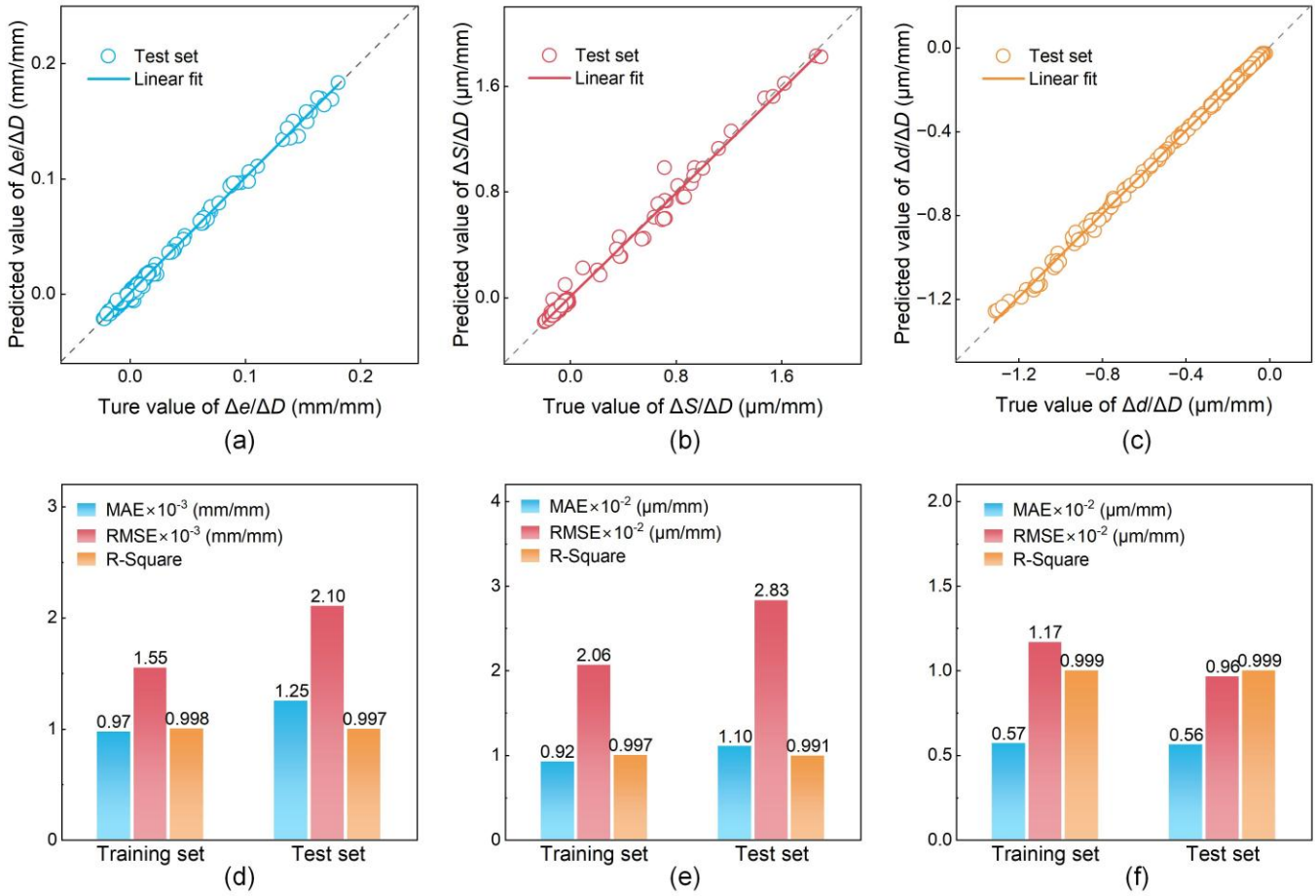

Fig. 5. Training results of the ANN models. (a) Comparison between predicted and actual values of $\Delta e/\Delta D$. (b) Comparison between predicted and actual values of $\Delta S/\Delta D$. (c) Comparison between predicted and actual values of $\Delta d/\Delta D$. (d) Performance metrics of the $\Delta e/\Delta D$ prediction model. (e) Performance metrics of the $\Delta S/\Delta D$ prediction model. (f) Performance metrics of the $\Delta d/\Delta D$ prediction model.

For the roundness error model (Fig. 6(a)), v has greater importance than D, whereas D contributes more than v in the grain size range model (Fig. 6(c)) and average grain size model (Fig. 6(e)). These results indicate that roundness error is more sensitive to process parameters, while microstructure indicators are mainly affected by the deformation amount during PRR, consistent with established domain knowledge [8,9].

Fig. 6(b), (d), and (f) illustrate the effects of input variables on model outputs. For the roundness error (Fig. 6(b)) and average grain size models (Fig. 6(f)), SHAP values increase with v, indicating that higher mandrel feed rates increase the predicted e and d. Thus, both e and d are positively correlated with v. In contrast, the SHAP value of the grain size range model (Fig. 6(d)) decreases with increasing v, indicating that higher feed rates reduce S. Therefore, S is negatively correlated with v. These results agree with the monotonicity analysis in Section 3.2 and reported domain knowledge [8,9].

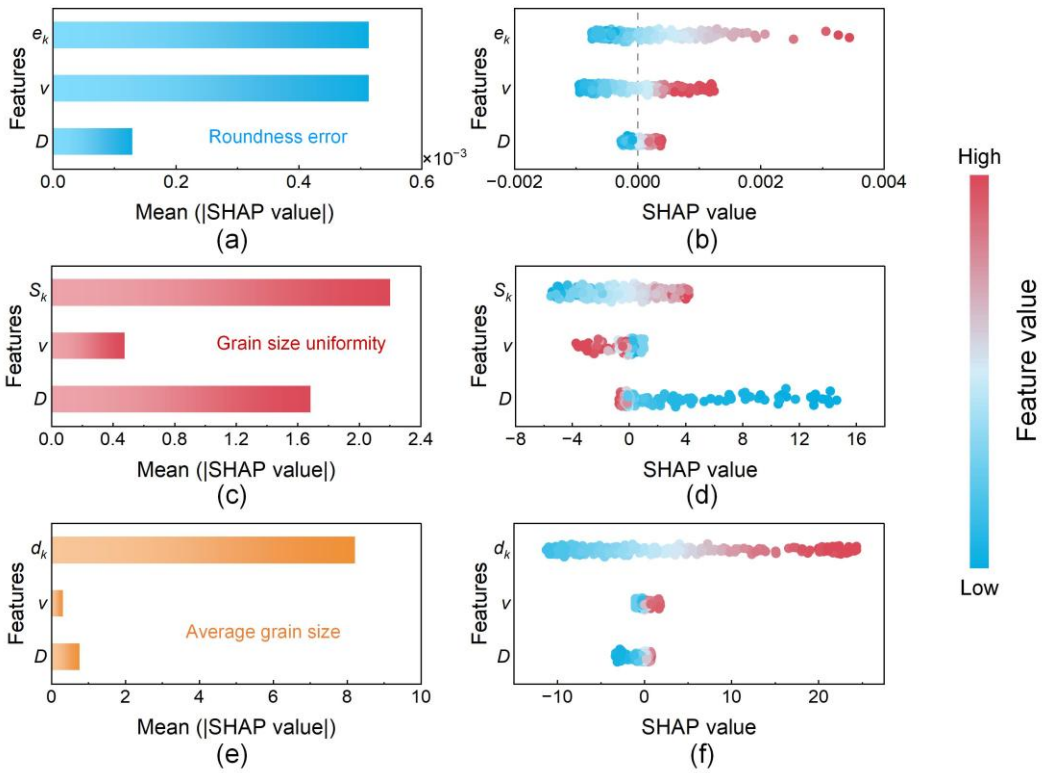

Fig. 6. SHAP interpretability analysis of the ANN models. (a) Feature importance ranking of the roundness error model. (b) SHAP summary plot for the roundness error model. (c) Feature importance ranking of the grain size range model. (d) SHAP summary plot for the grain size range model. (e) Feature importance ranking of the average grain size model. (f) SHAP summary plot for the average grain size model.

4.3 Model generalization and multi-step recursive prediction

Since MPC requires repeated multi-step predictions over a finite horizon, the accuracy of the ANN-based state equations must be maintained during prediction. To evaluate their suitability, multi-step predictions were performed on two cases not included in the training dataset. Case 1 used a constant mandrel feed rate of 2.0 mm/s, corresponding to the yellow dataset in Fig. 4. Case 2 used a linearly decreasing feed rate from 2.5 to 0.8 mm/s. The prediction results are shown in Fig. 7.

Fig. 7(a1)-(c1) and (a3)-(c3) present the full-horizon recursive predictions of the three ANN-based state equations. The initial states, reference diameter D, and mandrel feed rate v were obtained from the true simulation data, while subsequent states were recursively predicted using the developed models. A diameter increment of 10 mm was used, consistent with the training process. For both cases, all models achieved $R^2 >$ 0.8, indicating satisfactory multi-step prediction performance. The lower R^2 values in Fig. 7(a3) and (c3) indicate reduced accuracy as the prediction horizon increases due to accumulated errors in recursive prediction.

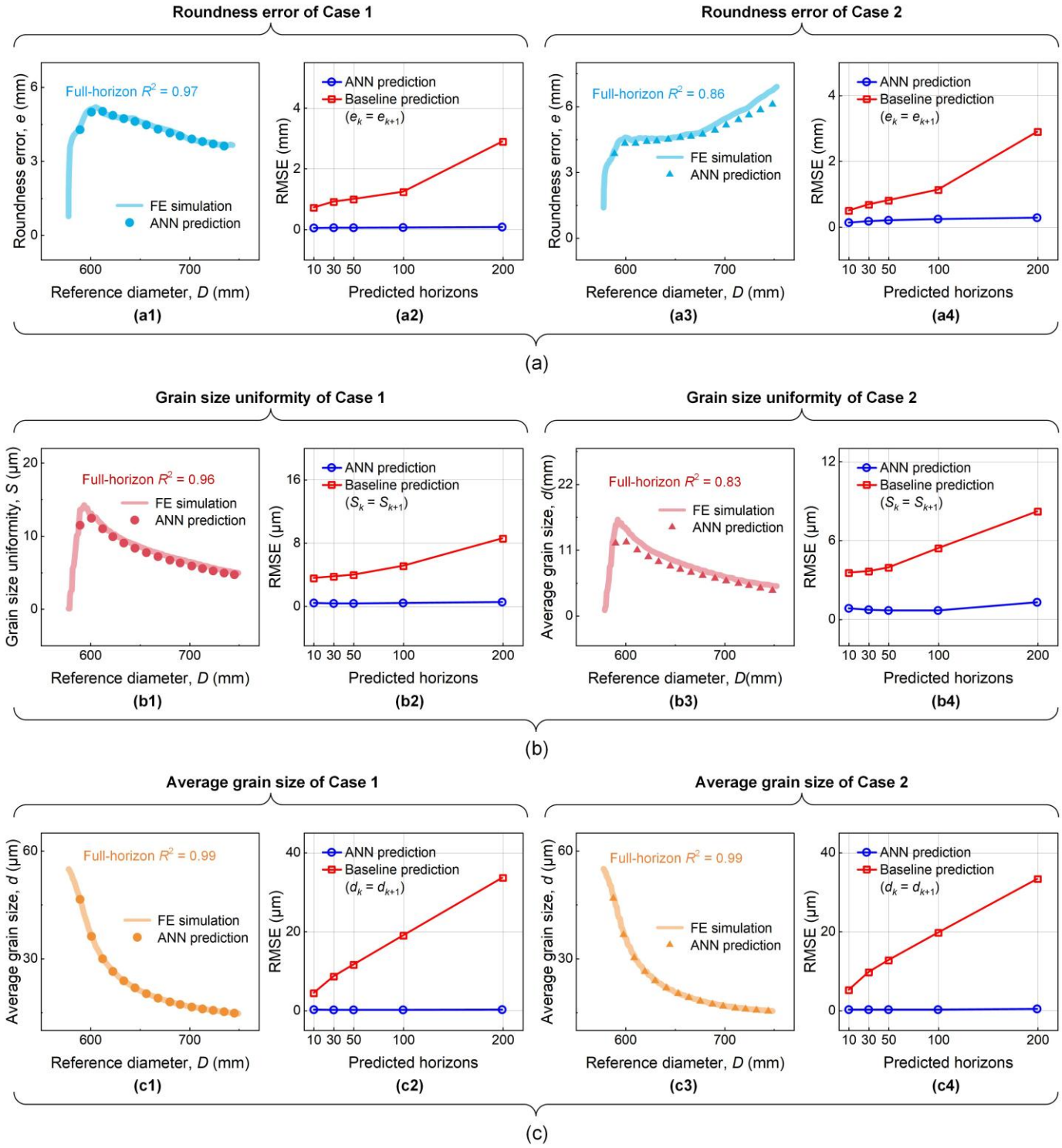

Fig. 7. Evaluation of recursive prediction capability of the ANN-based state equation. (a) Recursive prediction results for *e*. (b) Recursive prediction results for *S*. (c) Recursive prediction results for *d*.

Fig. 7(a2)-(c2) and Fig. 7(a4)-(c4) compare the RMSE values of the proposed ANN-based state equations with those of a baseline model under different prediction horizons (step size: 1 mm). In the baseline model, system states are assumed to remain unchanged. During prediction, states are recursively updated using the ANN-based equations, with the initial state corrected by the corresponding FE results at each prediction window. The ANN models consistently achieve lower RMSE values than the baseline model, demonstrating their ability to capture the effects of D and v on state evolution beyond historical state

information. Although RMSE increases with prediction horizon due to error accumulation, all models maintain high accuracy at a ten-step horizon (diameter increment of 10 mm). Therefore, a 10 mm prediction interval is adopted for the subsequent MPC implementation. These results confirm that the proposed ANN-based state equations provide sufficient prediction accuracy for the MPC framework.

5. Multi-objective control solving of the mandrel feed rate using ANN-MPC

5.1 Construction of state-dependent objective function

The primary MPC objectives are to minimize roundness error e, maintain average grain size d below 15.9 μm (ASTM Grade 9), and minimize grain size range S. As shown in Fig. 4, these states evolve continuously with strong path dependency; therefore, their objective terms are formulated as stage costs. The stage costs minimize the normalized deviations between predicted states and target values within each prediction horizon, as defined in Eqs. (12)-(14). Here, $e_{\max}$, $S_{\max}$, and $d_{\max}$ are the maximum values of e, S, and d during the process, respectively; e_t, S_t, and d_t are the target values; e_i, S_i, and d_i are the predicted states; and w_e, w_S, and w_d are weighting coefficients. To avoid abrupt velocity variations caused by non-smooth ANN gradients, a smoothing cost term is introduced in Eq. (15), where Δv is the velocity change between consecutive steps, $\Delta v_{\max}$ is the maximum allowable change, and $w_{\Delta v}$ is the weighting coefficient.

$$J_e = w_e\left(\frac{e_i - e_t}{e_{\max} - e_t}\right)^2 \tag{12}$$

$$J_S = w_s\left(\frac{S_i - S_t}{S_{\max} - S_t}\right)^2 \tag{13}$$

$$J_d = w_d\left(\frac{d_i - d_t}{d_{\max} - d_t}\right)^2 \tag{14}$$

$$J_{\Delta v} = w_{\Delta v}\left(\frac{\Delta v}{\Delta v_{\max}}\right)^2 \tag{15}$$

By summing the above cost terms, the total cost function of the MPC is given as Eq. (16). To ensure precise prediction of the system state at the end of the forming process ($D = D_f$), we introduce a horizon contraction mechanism. As the diameter D approaches the final target D_f, the prediction horizon N_k is gradually reduced, as defined in Eq. (17).

$$J = \sum_{i=0}^{N_k - 1}\left[J_e + J_S + J_d + J_{\Delta v}\right] \tag{16}$$

$$N_k = \min\left(N_{\max}, \left\lfloor \frac{D_f - D_k}{\Delta D} \right\rfloor\right) \tag{17}$$

Based on the physical knowledge in Section 3.2, the influence of the control variable v on system states (e, S, and d) varies with the forming stage. Therefore, the priority of control objectives changes during the process, making mandrel feed control in PRR a stage-dependent nonlinear optimization problem. To achieve adaptive control, a state-dependent weight function is proposed, as defined in Eqs. (18) and (19).

The weighting function adopts a softmax formulation to convert normalized state deviations into adaptive weights. Each weight is constrained to [0,1], and the weights sum to 1. The controller thus adjusts objective priorities according to current state deviations, assigning larger weights to states farther from their targets. In Eqs. (18) and (19), β denotes the sensitivity coefficient; a larger β increases weight differences and emphasizes the objective with the largest deviation.

$$\alpha = \frac{1}{\exp\left[\beta \max(0, \frac{e_i - e_{\mathrm{t}}}{e_{\max} - e_{\mathrm{t}}})\right] + \exp\left[\beta \max(0, \frac{S_i - S_{\mathrm{t}}}{S_{\max} - S_{\mathrm{t}}})\right] + \alpha \exp\left[\beta \max(0, \frac{d_i - d_{\mathrm{t}}}{d_{\max} - d_{\mathrm{t}}})\right]} \tag{18}$$

$$\begin{cases} w_e = \alpha \exp\left[\beta \max(0, \frac{e_i - e_{\mathrm{t}}}{e_{\max} - e_{\mathrm{t}}})\right] \\ w_S = \alpha \exp\left[\beta \max(0, \frac{S_i - S_t}{S_{\max} - S_{\mathrm{t}}})\right] \\ w_d = \alpha \exp\left[\beta \max(0, \frac{d_i - d_{\mathrm{t}}}{d_{\max} - d_{\mathrm{t}}})\right] \end{cases} \tag{19}$$

5.2 SQP-based solution of the mandrel feed rate optimization problem

In the PRR MPC optimization problem, the system state equations are imposed as equality constraints. To improve control stability, equipment-related constraints are also considered. The mandrel feed rate is constrained within the allowable range of the equipment, as defined in Eq. (20), where $v_{\min}$ and $v_{\max}$ denote the minimum and maximum feed rates, respectively. In addition, the feed rate variation between consecutive sampling instants is limited by $\Delta v_{\max}$, as expressed in Eq. (21). Therefore, the PRR MPC problem is formulated as a nonlinear programming problem in Eq. (22).

$$v_{\min} \le v_k \le v_{\max} \tag{20}$$

$$\left| v_{k+1} - v_k \right| \le \Delta v_{\max} \tag{21}$$

$$\min J = \sum_{i=0}^{N_k-1} \left[J_e + J_S + J_d + J_{\Delta v} \right]$$

$$s.t. \begin{cases} e_{k+1} = e_k + f(v_k, D_k, e_k)(D_{k+1} - D_k) \\ S_{k+1} = S_k + g(v_k, D_k, S_k)(D_{k+1} - D_k) \\ d_{k+1} = d_k + h(v_k, D_k, d_k)(D_{k+1} - D_k) \\ v_{\min} \le v_k \le v_{\max} \\ \left| v_{k+1} - v_k \right| \le \Delta v_{\max} \end{cases} \tag{22}$$

Sequential quadratic programming (SQP) is widely used to solve constrained nonlinear optimization problems. Due to its convergence and computational efficiency, SQP is adopted to solve the MPC problem in this study. At each sampling instant, SQP determines the optimal control sequence $\boldsymbol{v}^*$ by solving the MPC optimization problem in Eq. (23). Following the receding horizon strategy, only the first control action is applied, while the remaining actions are discarded. The applied mandrel feed rate is given by Eq. (24).

$$\boldsymbol{v}_k^* = [v_{0|k}^*, v_{1|k}^*, v_{2|k}^*, ..., v_{N-1|k}^*]^{\mathrm{T}} \tag{23}$$

$$v = \begin{cases} v_{\max} (D = D_0) \\ v_{0|k}^* (D_0 < D \le D_{\mathrm{f}}) \end{cases} \tag{24}$$

5.3 Tuning of weight parameters

The parameters to be optimized in the MPC framework are the sensitivity coefficient β and the smoothing weight $w_{\Delta v}$. To avoid time-consuming repeated FE simulations, we combine ANN-based offline simulation with Bayesian optimization (BO) for parameter tuning. Bayesian optimization utilizes Gaussian processes to guide the search, enabling the identification of a near-global optimum within a limited number of evaluations. The objective function for BO is defined in Eq. (25), while all other parameters remain identical to those used in the online MPC implementation.

$$score = \left[\frac{\max(0, e_{\mathrm{final}})}{e_{\max} - e_{\mathrm{t}}} \right]^2 + \left[\frac{\max(0, S_{\mathrm{final}})}{S_{\max} - S_{\mathrm{t}}} \right]^2 + \left[\left(\frac{\max(0, d_{\mathrm{final}})}{d_{\max} - d_{\mathrm{t}}} \right) \right]^2 \tag{25}$$

6. Online optimization of mandrel feed strategy using ANN-MPC-based digital twin FE model

6.1 Development of the ANN-MPC-based digital twin FE model for PRR

During PRR simulation, the system states (e, S, and d) are extracted in real time from the ABAQUS history output using Python scripts through the ABAQUS command interface. A polling interval of 5 s is adopted for state monitoring. The extracted system states are then transferred to the database, which consists of multiple independent CSV files in the present implementation. The ANN-MPC controller is developed in MATLAB to perform state prediction and optimization. After solving the optimization problem, the optimized control input (v) is written into a CSV file and retrieved by the VUAMP subroutine in ABAQUS.

The mandrel feed rate is then updated according to the optimized control input for the subsequent FE simulation step.

The proposed DTFEM integrates three aspects. (1) **Material digital twin:** the model accurately describes the evolution of grain size and grain size uniformity of IN718 alloy profiled rings during the rolling process (Fig. 3). (2) **Process digital twin:** the model reproduces the PRR process of the physical ring rolling equipment, including the blank and forged ring geometries, geometric evolution during forming (Fig. 3), and thermo-mechanical boundary conditions (Table 1). (3) **Control digital twin:** the model monitors ring roundness, grain size, and grain uniformity in real time through ABAQUS history outputs. The ANN-MPC controller predicts the future evolution of ring states over a finite horizon and optimizes the mandrel feed rate online by adaptively adjusting the weighting of control objectives according to the real-time state risks, achieving coordinated optimization of roundness, grain size, and grain uniformity.

6.2 Online optimization of mandrel feed strategy within a single simulation based on digital twin FE model

Using the ANN-MPC-based DTFEM established in Section 6.1, the mandrel feed strategy for the profiled ring (Fig. 4(a)) was optimized, with parameters listed in Table 3. The objective function surface obtained from ANN-BO is shown in Fig. 8. Better solutions are mainly located near the lower bounds of β and $w_{\Delta v}$, indicating that a smoother feed strategy improves the coordinated control of the three objectives. The objective function varies within a narrow range (approximately 0.64-0.71) across the parameter space, corresponding to only about 4% improvement in each objective, indicating low sensitivity to β and $w_{\Delta v}$. Therefore, the proposed ANN-MPC framework exhibits good robustness to parameter variations and reduces the need for extensive parameter tuning. The BO-optimized parameters are adopted in this study to achieve the best control performance.

The optimized mandrel feed strategy obtained from the ANN-MPC-based DTFEM (hereafter referred to as the MPC strategy) is shown in Fig. 9(a). This trend agrees with industrial experience in PRR, where a progressively decreasing feed rate is generally considered beneficial for rolling stability and ring roundness.

Fig. 9(b) compares the outer diameter growth rate of the ring under the MPC strategy and a constant feed strategy. To highlight the advantages of the MPC strategy, we selected a case with better overall quality (v = 1 mm/s) from Fig. 4 for comparison. During the intermediate and final rolling stages (640 mm < D < 750 mm), the MPC strategy maintains an approximately constant diameter growth rate of 4.5 mm/s, whereas the constant feed strategy shows a continuous increase. This demonstrates that the MPC strategy stabilizes diameter growth and reduces dynamic impact between the ring and rollers, thereby improving rolling stability, consistent with previous mandrel feed strategy studies [10,12].

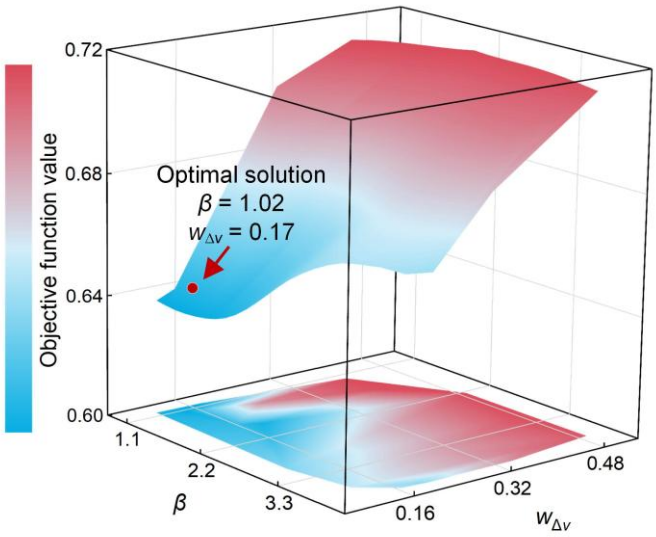

Fig. 8. The Bayesian optimization results of the MPC parameters.

Table 3. The parameters for ANN-MPC and ANN-BO.

Parameters	**Values**
Maximum mandrel feed speed, v_{max} (mm/s)	2.5
Minimum mandrel feed speed, v_{min} (mm/s)	0.5
Maximum variation of mandrel feed speed, Δv_{max} (mm/s)	0.2
Prediction step size, ΔD (mm)	1
Target value of roundness error, e_t (mm)	3
Target value of roundness error, S_t (μm)	7
Target value of mean grain size, d_t (μm)	15.9 (ASTM Grade 9) [36]
Maximum prediction horizon, N_{max}	10
Maximum grain size range, S_{max} (μm)	22
Maximum roundness error, e_{max} (mm)	7
Initial grain size, d_0 and d_{max} (μm)	55
Range of the sensitivity coefficient of the weighting function, β	[1,4]
Range of the smoothing weight, $w_{\Delta v}$	[0.1,1]

Fig. 9(c)-(e) compare the evolution of e, S and d under the MPC and constant feed strategies. As shown in Fig. 9(c), the MPC strategy reduces the roundness error in the later rolling stage by 28%, owing to the stabilized diameter growth rate (Fig. 9(b)). Fig. 9(d) shows that the MPC strategy improves grain uniformity, reducing the final grain size range by 33%. This improvement results from the higher feed rate in the early stage, which promotes deformation penetration through the blank thickness and produces a more uniform strain distribution, so that the recrystallized fraction in the core region approaches that in the surface region. As shown in Fig. 9(e), the average grain size under the MPC strategy is comparable to that under the constant feed strategy and approaches the minimum achievable value within the current process window (Fig. 4(e)). The rapid feed rate reduction in the early stage (Fig. 9(a)) maintains a high recrystallized fraction and

promotes grain refinement. Overall, the MPC strategy effectively balances roundness, grain uniformity, and grain refinement, enabling the production of higher-quality profiled rings within the available process window.

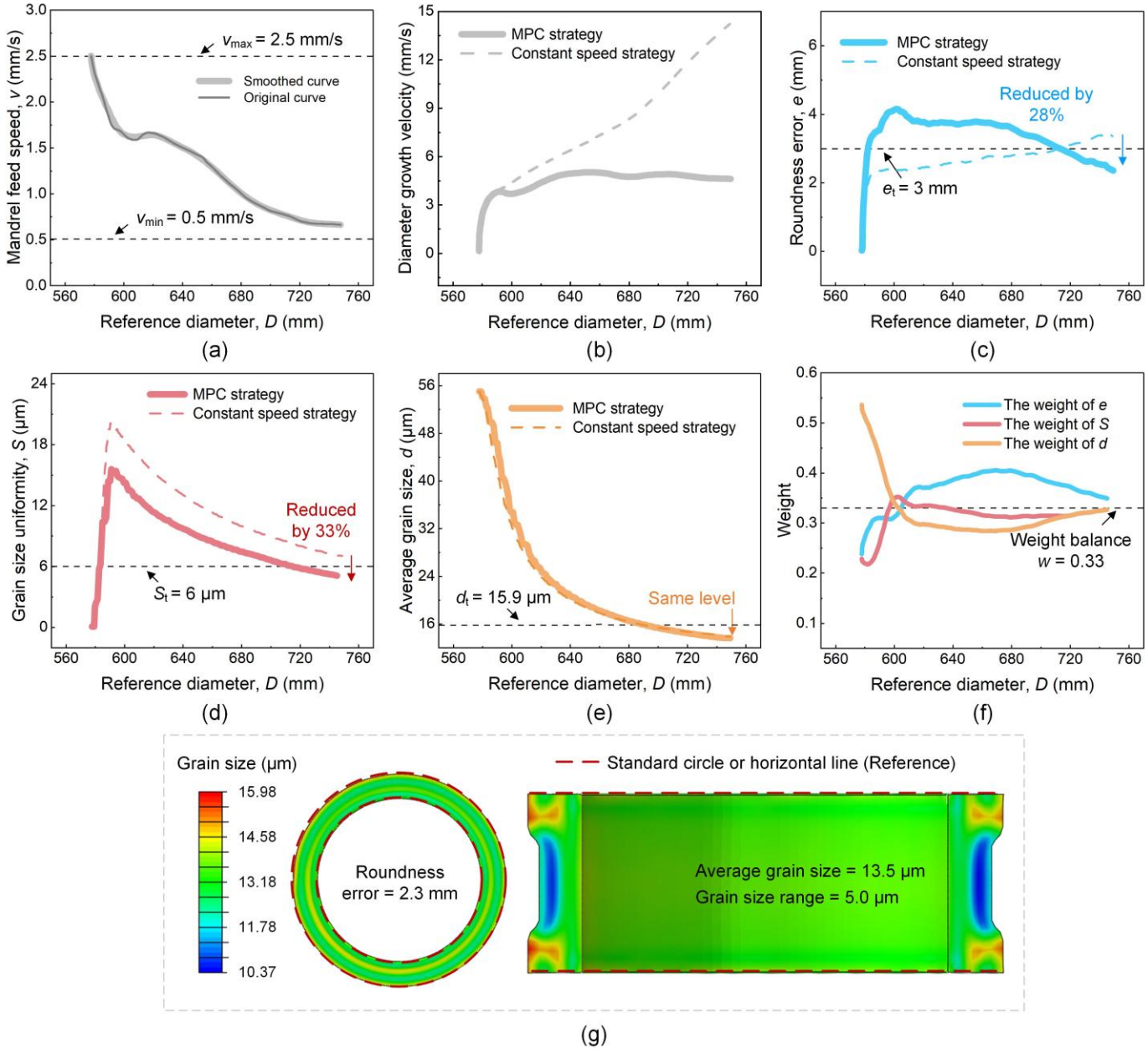

Fig. 9. Results of profiled ring rolling under the proposed MPC strategy. (a) Mandrel feed rate curve. (b) Outer diameter growth rate. (c) Evolution of roundness error. (d) Evolution of grain size range. (e) Evolution of average grain size. (f) Evolution of the weighting coefficients during PRR. (g) Profile of the ring formed using the MPC strategy. The dashed lines denote the corresponding results of the constant-feed case (v = 1.0 mm/s) presented in Fig. 4, serving as a benchmark for comparison with the proposed MPC strategy.

The evolution of the state-dependent weighting coefficients w_e, w_S, and w_d is shown in Fig. 9(f). During the early forming stage (578 mm < D < 590 mm), d exhibits the highest risk and receives the largest weight. Since d increases with v, the controller rapidly reduces the feed rate to promote grain refinement, consistent with Fig. 9(a). As rolling proceeds, the risk and weight of d decrease, while those of S increase and reach a

maximum near D = 600 mm. Because S decreases with increasing v, the controller maintains a relatively high feed rate during this stage to improve grain uniformity, resulting in the feed rate plateau observed in Fig. 9(a). In the later stage (620 mm < D < 750 mm), the risk and weight of e increase continuously. Since e increases with v, the controller further reduces the feed rate to improve roundness. Although S remains important, e is more sensitive to v at this stage (Fig. 6), and therefore becomes the dominant control objective, leading to a gradual feed rate reduction.

In summary, the evolution of the weighting coefficients is closely reflected in the resulting mandrel feed strategy. The controller automatically shifts its control focus among average grain size, grain size range, and roundness error according to the real-time system state, adjusting the feed rate in a physically meaningful manner. These results confirm that the proposed MPC framework is capable of autonomously evaluating system state risks and achieving coordinated control of geometric and microstructural quality in PRR. Consequently, a satisfactory profiled ring is produced (Fig. 9(g)).

7. Conclusion and future work

This study proposes an artificial neural network-based model predictive control (ANN-MPC) framework for profiled ring rolling (PRR) and uses it to develop a material-process-equipment integrated digital twin finite element model (DTFEM) for online optimization of the mandrel feed strategy. The main conclusions are summarized as follows:

(1) An ANN-MPC framework is proposed for PRR. The framework predicts the ring states over a finite prediction horizon based on the real-time geometric and microstructural states and optimizes the mandrel feed rate according to predefined forming objectives.

(2) ANN-based system state equations with embedded monotonicity constraints are established to describe the evolution of roundness error, average grain size, and grain size range during PRR. These equations demonstrate good prediction accuracy, satisfactory multi-step prediction performance, and interpretability, making them suitable as the prediction model for MPC.

(3) A state-dependent weighting strategy is proposed for adaptive multi-objective mandrel feed control. By dynamically adjusting the priority of the roundness error, average grain size, and grain size range according to the current state risk, coordinated control of the geometric accuracy and microstructure of the rolled ring is achieved.

(4) Based on the ANN-MPC framework, a DTFEM for PRR is developed by integrating material, process, and control digital twins, serving as a virtual representation of the physical ring rolling equipment. The DTFEM optimizes the mandrel feed strategy online within a single FE simulation, avoiding the offline

trial-and-error iterations required by conventional methods.

This work provides theoretical and technical support for the development of AI-driven ring rolling technology and intelligent ring rolling equipment. The proposed ANN-MPC-based DTFEM framework is applicable to different profiled ring rolling processes. In this work, a typical profiled ring rolling process was selected as the study subject to systematically clarify the development of an ANN-MPC-based DTFEM and its application in online optimization of the mandrel feed strategy. Future work will focus on expanding the training dataset to include structural parameters of different profiled rings, improving the generalization capability of the proposed framework. Furthermore, we will collaborate with equipment manufacturers to integrate the proposed method into the machine control system, enabling profiled ring rolling with online optimized feed strategies.

Reference

[1] Zou SJ, Li XC, Li F et al (2026) A stable forming condition for the whole spinning-rolling process of big-tapered profiled ring disk. Int J Adv Manuf Technol 145: 8971-9000. https://doi.org/10.1007/s00170-026-18848-2

[2] Allwood JM, Tekkaya AE, Stanistreet TF (2005) The development of ring rolling technology. *Steel Res Int* 76(2-3): 111-120. https://doi.org/10.1002/srin.200506044

[3] Han Y, Wang MH, Su H et al (2024) Optimizing profiled ring preforms for enhanced deformation uniformity using the isothermal field method. Thin Wall Struct 202: 112140. https://doi.org/10.1016/j.tws.2024.112140

[4] Wang X, Wen T, Wang LX et al (2026) Manufacturing large-tapered profile rings by combination of flaring and confined axial ring rolling processes. J Manuf Process 164: 263-278. https://doi.org/10.1016/j.jmapro.2026.02.049

[5] Zheng G, Wang X, Huang K et al (2025) A multi-sensor information fusion method for measuring geometric states in ring rolling processes. J Manuf Process 149: 664-678. https://doi.org/10.1016/j.jmapro.2025.05.011

[6] Lee KH, Kim BM (2013) Advanced feasible forming condition for reducing ring spreads in radial-axial ring rolling. Int J Mech Sci 76: 21-32. https://doi.org/10.1016/j.ijmecsci.2013.08.007

[7] Xie D, Ouyang Q, Wang Y et al (2023) Radial-axial feeding process design for large-scale flat ring by quantitative estimation of ring roundness error. Thin Wall Struct 189: 110887. https://doi.org/10.1016/j.tws.2023.110887

[8] Zhu XL, Liu D, Xing LJ et al (2016) Microstructure evolution of Inconel 718 alloy during ring rolling

process. Int J Precis Eng Manuf 17: 775-783. https://doi.org/10.1007/s12541-016-0095-8

[9] Tang XF, Wang BY, Zhang H et al (2017) Study on the microstructure evolution during radial-axial ring rolling of IN718 using a unified internal state variable material model. Int J Mech Sci 128: 235-252. https://doi.org/10.1016/j.ijmecsci.2017.04.023

[10] Guo LG, Yang H (2011) Towards a steady forming condition for radial-axial ring rolling. Int J Mech Sci 53(4): 286-299. https://doi.org/10.1016/j.ijmecsci.2011.01.010

[11] Hua L, Qian DS, Pan LB (2009) Deformation behaviors and conditions in L-section profile cold ring rolling. J Mater Process Technol 209(11): 5087-5096. https://doi.org/10.1016/j.jmatprotec.2009.02.007

[12] Yan FL, Hua L, Wu YQ (2007) Planning feed speed in cold ring rolling. Int J Mach Tool Manuf 47(11): 1695-1701. https://doi.org/10.1016/j.ijmachtools.2007.01.009

[13] Li L, Zhang T, Liu F et al (2026) Target contour extraction framework for ring rolling process based on machine vision. Int J Adv Manuf Technol 2026; 145, 3295-3316. https://doi.org/10.1007/s00170-026-18473-z

[14] Ge SC, Wu YX, Long ZY et al (2024) Position/force control method for profiled ring rolling process of large aluminum alloy ring. CIRP J Manuf Sci Technol. 51: 342-356. https://doi.org/10.1016/j.cirpj.2024.05.006

[15] Liang L, Guo LG (2022) Advanced feeding strategy driven by staged growth velocity for groove-section profiled ring rolling. J Manuf Process 81: 907-921. https://doi.org/10.1016/j.jmapro.2022.07.050

[16] Xu WJ, Chen F, Guo ZQ et al (2017) Parametric design of ring billet for profile ring rolling process based on electric field method and feeding strategy design. Int J Adv Manuf Technol 93: 1017-1027. https://doi.org/10.1007/s00170-017-0530-8

[17] Liang L, Zou CJ, Guo LG (2024) Forming process chain for manufacturing complex conical-section profiled rings: On a co-design method. Chin J Aeronaut 37(6): 485-503. https://doi.org/10.1016/j.cja.2023.12.024

[18] Han Y, Wang MH, Su H et al (2025) Adaptive PID control and process optimization for mandrel motion in profiled ring rolling. J Manuf Process 145: 410-425. https://doi.org/10.1016/j.jmapro.2025.04.075

[19] Chen F, Tian X, Liu ZX et al (2025) A novel continuous dynamic recrystallization model to reveal grain refinement mechanism in constraining ring rolling of thin-walled conical structure with inner

ribs. Int J Mach Tool Manuf 206: 104255. https://doi.org/10.1016/j.ijmachtools.2025.104255

[20] Liang L, Guo LG, Wang YF et al (2019) Towards an intelligent FE simulation for real-time temperature-controlled radial-axial ring rolling process. J Manuf Process 48: 1-11. https://doi.org/10.1016/j.jmapro.2019.09.032

[21] Liang L, Guo LG, Li XC et al (2018) Intelligent simulation for real-timely force-controlled radial-axial rolling process of supersized aluminium alloy rings. Procedia Manuf 15: 105-112. https://doi.org/10.1016/j.promfg.2018.07.183

[22] Wang J, Xie YF, Xie SW et al (2024) Development of data-knowledge-driven predictive model and multi-objective optimization for intelligent optimal control of aluminum electrolysis process. *Eng Appl Artifi Intell* 134: 108664. https://doi.org/10.1016/j.engappai.2024.108664

[23] Mehraban Z, Zadeh AY, Khayyam H et al (2024) Fuzzy adaptive cruise control with model predictive control responding to dynamic traffic conditions for automated driving. Eng Appl Artifi Intell 136: 109008. https://doi.org/10.1016/j.engappai.2024.109008

[24] Wang Z, Zhang J, Wang Z et al (2025) Research on optimization strategy for steel strip temper rolling elongation based on model predictive control. Eng Appl Artifi Intell 159: 111785. https://doi.org/10.1016/j.engappai.2025.111785

[25] He A, Wang CH, Liu S et al (2020) Switched model predictive path control of incremental sheet forming for parts with varying wall angles. J Manuf Process 53: 342-355. https://doi.org/10.1016/j.jmapro.2020.02.012

[26] Wang CH, He A, Liu S et al (2023) Learning-based model predictive control for two-point incremental sheet forming. J Manuf Process 105: 187-198. https://doi.org/10.1016/j.jmapro.2023.09.040

[27] Deng JD, Mao HJ (2015) A blank optimization design method for three-roll cross rolling of complex-groove and small-hole ring. Int J Mech Sci 93: 218-228. https://doi.org/10.1016/j.ijmecsci.2014.10.024

[28] Lee S, Park J, Kim N et al (2023) Extreme gradient boosting-inspired process optimization algorithm for manufacturing engineering applications. Mater Des 226: 111625. https://doi.org/10.1016/j.matdes.2023.111625

[29] Lee S, Lim Y, Galdos L et al (2024) Gaussian process regression-driven deep drawing blank design method. Int J Mech Sci 265: 108898. https://doi.org/10.1016/j.ijmecsci.2023.108898

[30] Gao PF, Li XS, Yan XG, et al (2025) Digital twin-driven intelligent spinning technique for curved

surface parts. J Ind Inf Integr 45: 100848. https://doi.org/10.1016/j.jii.2025.100848

[31] Gao PF, Yan XG, Wang Y et al (2023) An online intelligent method for roller path design in conventional spinning. J Intell Manuf 34: 3429-3444. https://doi.org/10.1007/s10845-022-02006-y

[32] Xia QX, Zhao J, Xiao GF et al (2026) A CNN-LSTM model for strain-geometry state prediction and defect control in multi-pass flow forming of thick-walled tubes. J Intell Manuf. https://doi.org/10.1007/s10845-026-02793-8

[33] Jung M, da Costa Mendes PR, Önnheim M et al (2023) Model predictive control when utilizing LSTM as dynamic models. *Eng Appl Artifi Intell* 123: 106226. https://doi.org/10.1016/j.engappai.2023.106226

[34] Liang L (2023) Regulation mechanism of precision forming and microstructure for IN718 alloy typical profiled ring rolling. Dissertation, Northwestern Polytechnical University [Chinese].

[35] Li HT, Guo LG, Li H et al (2025) Competitive behaviors and oriented control strategies of metal flow in profiled ring rolling. J Mater Process Technol 346: 119125. https://doi.org/10.1016/j.jmatprotec.2025.119125

[36] ASTM Standard E112-25(2025) Standard test methods for determining average grain size. ASTM International. https://doi.org/10.1520/E0112-25.

Statements & Declarations

Funding

The authors acknowledge the funding support from the National Natural Science Foundation of China (52275378, 52675510). Author Lianggang Guo has received research support.

Competing Interests

The authors have no relevant financial or non-financial interests to disclose.

Author Contributions

Haotian Li: Investigation, Methodology, Software, Visualization, Writing - original draft. **Lianggang Guo:** Conceptualization, Formal analysis, Funding acquisition, Supervision, Writing - review & editing. **Hao Deng:** Project administration, Validation. **Hengjun Luo**: Project administration, Validation. **Heng Li:** Project administration, Supervision.

Acknowledgments

The authors acknowledge the funding support from the National Natural Science Foundation of China (52275378, 52675510).

Supplementary Files

This is a list of supplementary files associated with this preprint. Click to download.

- GraphicalAbstract.docx
- Highlights.docx